Reduced-Dose Imageless Needle and Patient Tracking in Interventional CT Procedures

G. Medan and L. Joskowicz, *Fellow, IEEE*

***Abstract*— This paper describes a new method for imageless needle and patient tracking in interventional CT procedures based on fractional CT scanning. Our method accurately locates a needle with a spherical marker attached to it at a known distance from the tip with respect to the patient in the CT scanner coordinate frame with online sparse scan sampling and without reconstructing the CT image. The key principle of our method is to detect the needle and attached spherical marker in projection (sinogram) space based on the strongly attenuated X-ray signal due to the metallic composition of the needle and the needle's thin cylindrical geometry, and based on the marker's spherical geometry. A transformation from projection space to physical space uniquely determines the location and orientation of the needle and the needle tip position. Our method works directly in projection space and simultaneously performs patient registration and needle localization for every fractional CT scanning acquisition using the same sparse set of views. We performed registration and needle tip localization in five abdomen phantom scans using a rigid needle, and obtained a voxel-size tip localization error. Our experimental results indicate a voxel-sized deviation of the localization from a comparable method in 3-D image space, with the benefit of allowing X-ray dose reduction via fractional scanning at each localization. This benefit enables more frequent tip localizations during needle insertion for a similar total dose, or a reduced total dose for the same frequency of tip localization.**

***Index Terms*— Interventional CT, fractional CT scanning, reduced dose CT scanning, needle tracking, radon space registration.**

I. Introduction

INTERVENTIONAL CT procedures are nowadays common and rapidly increasing. During the intervention, CT imaging is repeatedly performed to determine the location of an incrementally inserted instrument with respect to the patient anatomy. The main disadvantage of CT imaging is that it exposes the patient to substantial X-rays ionizing radiation, which has been show to increase the risk of carcinogenesis [1]–[3]. Consequently, radiation dose reduction is a key issue. In CT imaging, the basic trade-off is between radiation dose and image quality. Lower doses produce imaging artifacts and increased noise, thereby reducing the image quality and limiting its clinical usefulness. This issue is exacerbated in interventional CT, where repeated scanning is performed during an intervention. This limits the number of scans that can be acquired, thus restricting the surgeon control and hampering the technical success rate of the intervention [4].

Various techniques are currently available for interventional needle procedures, including ultrasound imaging, X-ray fluoroscopy, CT scanning with optical guidance or tracking of manual insertion, and robotic needle steering using CT, ultrasound, or X-ray imaging for guidance. Needle localization methods in CT typically require the needle to be aligned with the plane of imaging (in-plane imaging) [5].

Dose reduction techniques in CT include patient-specific tube current modulation, step-and-shoot methods, and statistical reconstruction of low-dose scans. A significant radiation exposure reduction with deteriorated but diagnostically acceptable image quality can be achieved with these methods. Most methods assume that the CT scan is stand-alone and independent of previously acquired patient CT scans, while others aim at repeat scan image reconstruction using information from previous scans.

Another approach for reducing the radiation dose in a single scan is the selective acquisition of a fraction of scan angles, referred to as fractional, sparse-view, or few-view CT scanning. In this approach, the patient is exposed to a fraction of the radiation that is required for a full scan by reducing the number of scan angles. However, since part of the projection data is missing, severe streaking artifacts appear in the image. Different methods have been developed to reduce and/or compensate for imaging artifacts to produce clinically acceptable results [6]–[10]. The feasibility of this approach, which in not currently available in commercial CT scanners, has also been investigated. Fractional scanning could be achieved, for instance, by alternating the voltage and tube current between high and low values at different scan angles, thus substantially reducing the absorbed radiation at unnecessary angles [7].

II. Previous Work

Needle localization in CT imaging has been addressed in a variety of ways. Since the needle is localized in image space, the needle is often required to be inserted in the axial imaging (in-plane insertion), which forces the radiologist to adjust the gantry angle repeatedly and rescan until a suitable orientation is found [11]. Steering the needle inside the tissue toward the target can be achieved manually by the radiologist

Manuscript received July 15, 2017; revised August 15, 2017; accepted August 15, 2017. Date of publication August 21, 2017; date of current version November 29, 2017. This work was supported by Kamin, Office of the Chief Scientist, Ministry of Trade and Industry, Israel, under Grant 57706. *(Corresponding author: G. Medan.)*

The authors are with the CASMIP Laboratory, School of Computer Science and Engineering, The Hebrew University of Jerusalem, Jerusalem 9190401, Israel (e-mail: gmedan@cs.huji.ac.il; josko@cs.huji.ac.il).

Color versions of one or more of the figures in this paper are available online at http://ieeexplore.ieee.org.

Digital Object Identifier 10.1109/TMI.2017.2742898

under passive guidance, or by robotic steering in closed loop with the imaging. A commercial CT navigation device, SimpliCT by NeoRad [12], implements laser steering to guide the radiologist during manual insertion by aligning the needle with the laser direction. In [13], an optical tracking system uses surface markers to allow feedback of the needle orientation during the intervention. Another approach is to optically overlay the CT image on top of the patient using a semitransparent mirror, thereby providing the physician with visual guidance during manual needle insertion [14]. A robotic steering method described in [15] drives the needle based on a tissue interaction model and in-plane imaging to provide feedback for closed loop control of the insertion.

Note that all these methods rely on the acquisition of a full repeat scan and reconstruction of the image for each localization, with the associated cost in radiation dose for the patient. In the following section, we present a novel imageless method for needle localization in projection space using fractional scanning, which promises to reduce the radiation dose associated with each needle localization.

III. Materials and Methods

We describe next a new method for imageless needle and patient tracking in interventional CT procedures based on fractional CT scanning. Our method accurately locates a needle with a spherical marker attached to it at a known distance from the tip with respect to the patient in the CT scanner coordinate frame with online sparse scan sampling and without reconstructing the CT image. The key principle of our method is to detect in projection (sinogram) space the needle and spherical marker based on the needle strong X-ray signal and its thin cylinder geometry and the spherical marker center mounted on the needle. A transformation from projection space to physical space uniquely determines the location and orientation of the needle and the needle tip position. Our method works directly in projection space and simultaneously performs patient registration and needle localization for every fractional CT scanning acquisition.

The rest of this section is organized as follows. Section A provides a short background on the imaging characteristics of metallic objects in CT scanning. Section B describes the method materials, the composition and geometry of the spherical marker. Section C describes the projection space needle and marker localization method. Sections D and E elaborate on two key technical aspects of the method: needle and sphere localization in projection space and in 3D physical space.

A. Metallic Objects in CT Projection Space

When imaging a metallic object, the detector elements of a CT scanner which are behind the object relative to the X-ray source suffer from beam hardening or photon starvation, i.e., low energy photons are more easily attenuated by the metal, resulting in the detected number of photons not following the simple exponential decay of soft tissue attenuation [16]. This leads to a signal in projection space that does not represent the true attenuation integral of the source-detector ray path. As a consequence, image reconstruction based on this starved signal will produce non-local streak imaging artifacts which obscure the details of the metal object and its surroundings.

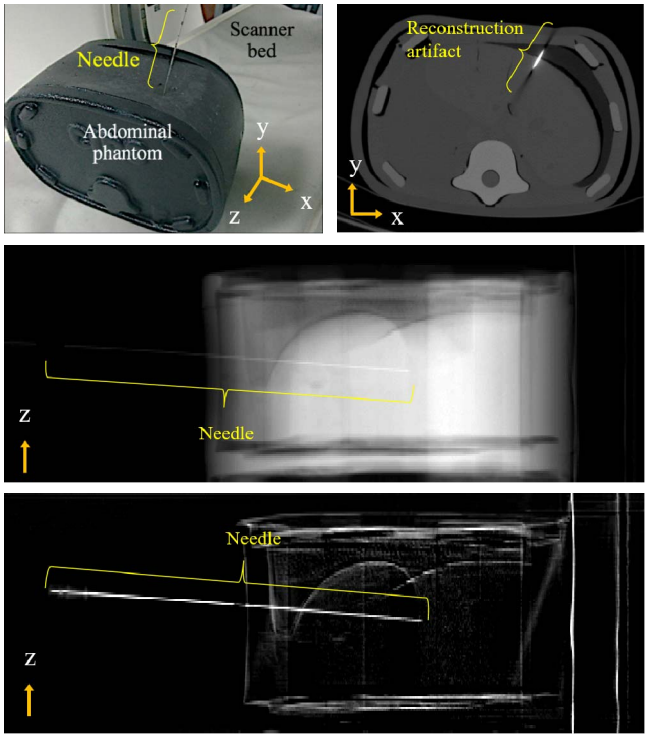

Fig. 1. Top left: needle inserted into GE abdominal phantom on CT scanner bed; Top right: reconstruction artifact caused by presence of the metallic needle, in axial view; Center: single projection view showing the needle inserted into the phantom; Bottom: projection difference between repeat scan with needle and aligned baseline scan for same view. The projection difference image contains bright lines in addition to the needle, mostly where physical edges in the object are projected onto the detector array, which is due mostly to small registration error.

In contrast, in projection space, photon starvation artifacts caused by metallic elements are local in nature. Thus, they can be accurately detected as the difference between a baseline projection in which the needle is absent, and an aligned repeat scan projection in which the needle is present (see Fig. 1). Furthermore, the repeat scan can be of a lower dose, limited scanning range and/or subsampled from selective views, since reconstruction of the repeat scan is not required. Our method therefore takes advantage of the strong needle signal in projection space to locate it and then transform its location in physical space based on the scanner imaging characteristics.

B. Materials

To determine the needle tip location accurately, we cannot rely solely on the projection difference data in the needle tip vicinity, as this data is noise-prone and suffers from partial volume effect since the slice intervals and/or the slice thickness is a few millimeters, which is often greater than the required accuracy. To address this issue, we attach to the needle a ceramic sphere of diameter several times larger than the needle diameter. The sphere is rigidly attached at a known distance from the needle tip, a distance larger than the expected insertion depth of the needle into the patient's body.

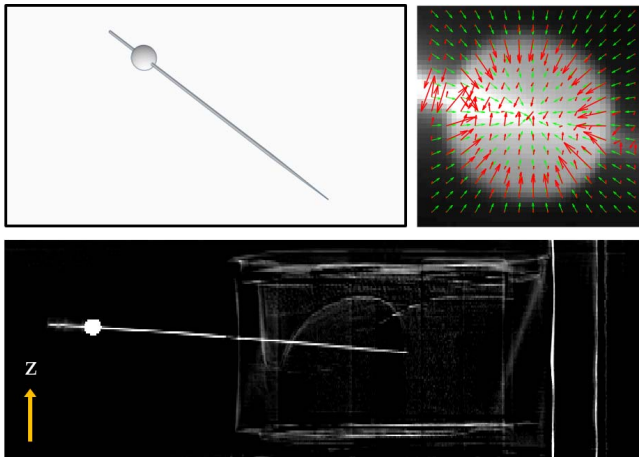

Fig. 2. Top left: model of needle with spherical marker; Bottom: projection difference image for single view, showing the marker as a bright circle and the needle as a straight line through its center; Top right: illustration of the marker localization method – bold arrows indicate the gradient, and thin arrows indicate the radial direction. The center is localized by minimizing a cost function aligning the two vector fields.

This sphere, which remains outside the patient body at all times, appears as a circle in projection space and is thus identifiable using pattern matching techniques. The accurate localization of the sphere in physical space allows tracing the known distance of the spherical marker along the needle path to determine the tip location. Fig. 2 shows a model of the needle with a sphere mounted on it and a projection difference image with the needle inserted.

C. Method

The input to the repeat scan needle location method is a dense baseline CT scan without the needle, which can be acquired preoperatively or intraoperatively. The main steps of the method are:

1) Acquisition of a sparse repeat CT scan with the needle and marker in current location using fractional scanning.
2) 3D Radon space registration of the sparse CT scan to the baseline CT scan based on the algorithm presented in [7].
3) Localization of the needle and marker in projection space.
4) Localization of the needle and marker in physical space and with respect to the baseline CT scan from its location in projection space.
5) Display of the current location of the needle with respect to the baseline scan in a 2D multi-slice image or a 3D image.

Steps 1-5 are repeated until the desired target structure inside the patient is reached. Optionally, one or two control CT scans for image reconstruction can be acquired during the procedure as needed.

A key aspect of our method is that it uses the same sparse projection sampling pattern both for registration and for needle localization. Thus, no additional scanning and no image reconstruction is necessary for metal element localization, so the radiation dose is a fraction of that required in image based methods. This allows repeated needle insertion and localization for better feedback and accuracy without excessive radiation dose.

The Radon-space rigid registration method (step 2, described in [7]) computes the rigid registration transformation between the baseline and repeat scan using the same sparse projection data obtained by fractional scanning used in the following stages. The method works by matching one-dimensional projections obtained via summation along parallel planes of both the baseline scan and the repeat scan, in a 3D extension of the 2D Radon transform. The calculation is performed entirely in projection space, and the matching is done based on maximization of normalized cross correlation. The matched projections are then used in order to construct a set of equations, the solution of which gives the parameters of the rigid registration between the scans.

We describe next the two key steps of our method: needle localization in projection space (step 3) and in physical space (step 4). Step 2 is performed using the method described in [7]. This method computes the rigid registration transformation between the baseline and repeat scan using the same sparse projection data obtained by fractional scanning used in the following stages.

In the following, lower-case letters denote 2D points and lines in the 2D projection space for a specific view – the angle at which the source is found. Upper-case letters denote 3D point, as well as lines and planes in physical space. A tilde ($\sim$) above a letter denotes homogenous coordinates, i.e. $\tilde{M} = [M_x, M_y, M_z, 1]^T$.

D. Needle Localization in Projection Space

Detectors which record a highly attenuated signal due to a metal element blocking the ray from the source are identified and localized by comparing the fractional repeat scan projection data to the baseline projection using the 3D rigid registration parameters computed in step 2. In this step, we compute a re-projection of the baseline CT scan such that the re-projected baseline data is aligned with the fractional repeat scan projection data of the inserted needle. For each view angle, we obtain a 2D projection difference image by subtracting the aligned projections so that only the differences are visible, most prominently the needle with the spherical marker. The size (in pixels) of this image is determined by the size of detector array, in which detectors readings are higher where their corresponding source-to-detector ray passes through the needle (See Fig. 2).

The needle localization in projection space proceeds in two steps. First, we localize the center c_i of the projected spherical marker roughly in each of the views $i = 1, \ldots, m$ by matching the difference projection image with a circle pattern via 2D cross-correlation. We then refine the localization by optimizing a cost function for each view as follows:

$$c_i = argmin_{c \in \mathbb{R}^2} \sum_{x:|\|x-c\|-R|<\varepsilon} \nabla h_i(x) \cdot \hat{r} \qquad (1)$$

where $h_i(x)$ is the projection difference image for view i, R is the known radius of the marker, and ε is a small distance constant (0.5 mm), so that the gradient of the projection difference image is best aligned with the radial

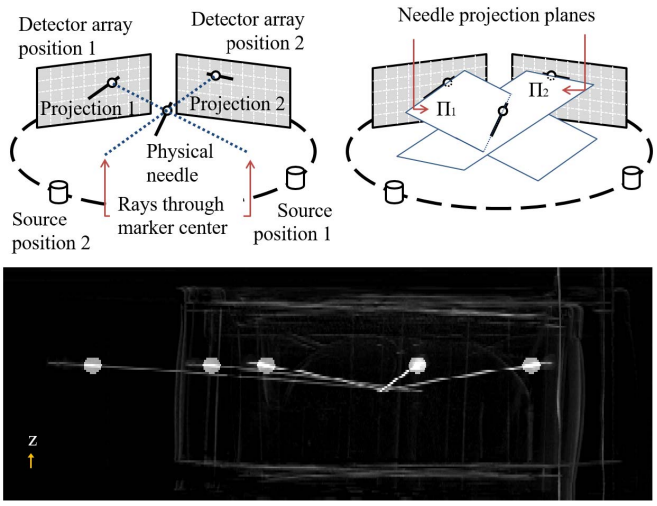

Fig. 3. Top: illustration of marker location as intersection of rays (left) and needle orientation as intersection of planes (right). Bottom: overlay of several representative fractional projection difference images showing both the needle and the marker as a circle and line (bright pixels) intersecting it.

direction $\hat{r} = (x - c) / \|x - c\|$ inside a ring of radius R and thickness 2ε. This cost function allows avoiding the high intensities due to the needle passing through the marker, while taking into account the relatively weaker gradients at the edge of the projected marker circle.

Second, we fit a 2D line l_i through the previously detected marker center c_i in each projection difference image, so that it is aligned with the projection of the needle which appears as a high intensity thin line (see Fig. 1). This is achieved by selecting the direction maximizing the accumulated intensity of the difference image along it. Specifically, we denote W_θ a thin rotating window of width ε and length D_{MT} (where D_{MT} is the known marker center distance from the tip of the needle), which is rotated by an angle θ in 2D about its end c_i. To find the line l_i we maximize the following cost function and find its slope angle θ_i:

$$\theta_i = argmax \sum\nolimits_{x \in W_\theta} h_i(x) \tag{2}$$

E. Needle Localization in Physical Space

Needle localization is achieved in three stages. First, we find the orientation, e.g., the line in physical space along which the needle is positioned. Then, we localize the spherical marker in physical space to establish an anchor along the needle line. Finally, the tip position is derived using the previously established line orientation and marker position.

1) Orientation in Physical Space: Each line l_i in a 2D projection as described above defines a line L_i on the plane of detector elements in physical space through the elements associated with the line l_i. The set of rays between each detector element position on L_i and the source position for view i define a plane Π_i in physical space. In parallel beam geometry, the source position is located at infinity and the set of rays are parallel. In cone-beam geometry, the set of rays forms a fan emanating from the source. Fig. 3 illustrates the case of parallel beam geometry.

In both parallel and cone beam geometries, the set of planes $\{\Pi_i\}$ forms a pencil of planes intersecting at a single line in physical space having an orientation vector $\hat{O}$ that corresponds to the needle orientation. We denote the plane normal vector $\hat{n}_i$. Since $\hat{O}$ is contained in all planes $\{\Pi_i\}$, the following set of equations holds:

$$\hat{O}^T \hat{n}_i = 0, \quad i = 1, \ldots, m \tag{3}$$

We solve this over-constrained system of equations by approximating the null-space of $\mathbf{N} = \left[\hat{n}_1\ \hat{n}_2 \ldots \hat{n}_m\right]^T$ using Singular Value Decomposition (SVD). Let $\mathbf{N} = U \Sigma V^T$ where U, V are orthonormal matrices and Σ has the singular values of $\mathbf{N}$ on its diagonal. Then, the columns of V corresponding to the smallest values on the diagonal of Σ are the basis to the approximate null-space. Since the planes $\{\Pi_i\}$ intersect at a line, the null-space is one-dimensional line in 3D physical space. Therefore, the column of matrix V corresponding to the smallest singular value in Σ is the solution. To improve robustness, we use the RANSAC scheme and compute the null-space for a random subset of rows of $\mathbf{N}$ at each iteration. We then select the result with most "supporters", i.e., the result for which most of the rows of $\mathbf{N}$ are nearly orthogonal to the considered null-space.

2) Marker Localization in Physical Space: Each projected marker center c_i is related to the physical marker center M by a projection matrix $P_i \in \mathbb{R}^{3\times4}$:

$$P_i \tilde{M} = \lambda_i \tilde{c}_i \quad i = 1, \ldots, m \tag{4}$$

where λ_i is an unknown scalar, and the projection matrix P_i for view angle i is computed from the known CT scanner geometry. Following [17], this set of equations can be re-written in matrix form as follows:

$$\underbrace{\begin{bmatrix} p_1 & \tilde{c}_1 & 0 & \cdots & 0 \\ p_2 & 0 & \tilde{c}_2 & \cdots & 0 \\ \vdots & \vdots & \vdots & \ddots & 0 \\ p_m & 0 & 0 & 0 & \tilde{c}_m \end{bmatrix}}_{H} \begin{bmatrix} \tilde{M} \\ -\lambda_1 \\ -\lambda_2 \\ \vdots \\ -\lambda_m \end{bmatrix} = \begin{bmatrix} 0 \\ 0 \\ 0 \\ \vdots \\ 0 \end{bmatrix} \tag{5}$$

We repeat the null-space calculation for the matrix $H \in \mathbb{R}^{3m\times(m+4)}$ to obtain the vector M by dividing the first three entries of the result by the fourth:

$$M = \left[\tilde{M}_1, \tilde{M}_2, \tilde{M}_3\right]^T / \tilde{M}_4$$

3) Tip Localization in Physical Space: Once the needle orientation $\hat{O}$ and the marker position M are established, the tip is localized by tracing the known distance between the tip and the marker along the needle orientation starting from the marker position. Assuming the needle is rigid and can be modeled as a straight line, the tip position T is defined by:

$$T = M + D_{MT} \hat{O} \tag{6}$$

where D_{MT} is the known marker center distance from the tip of the needle.

Fig. 4. Photograph of a needle with spherical marker attached to it at a known distance from the needle tip.

IV. Results

To demonstrate our method, we designed and conducted the following experiment on real CT scan data. We used a CIRS Model 57 abdomen phantom and a 16 Gauge (1.65 mm diameter) 25 cm rigid needle with a spherical marker attached to it at 200 mm from the needle tip (Fig. 4). The CT scanning was performed by GE Healthcare, Tirat HaCarmel using a GE Discovery CT750HD scanner. The dataset consists of 5 CT scans with both projection and image data of the abdomen phantom (Fig. 1, top) scanned with a needle inserted at different locations, depths and at different phantom positions, as well as one baseline scan without the needle present.

The reconstructed image size is $800\times800\times126$ voxels, with spatial resolution of $0.58\times0.58\times1.25$ mm^3. The detector array consists of 885×126 elements scanned at 984 views at regular intervals in the range [0°, 360°], where four slices were acquired in each full revolution. The data was re-binned from fan-beam to parallel rays' representation of the projections. The spherical marker had a diameter of 20mm and was affixed at 200mm from the tip.

The projection datasets were processed as follows:

1) We subtracted a full scan of the scanning bed without the phantom from the other scans, to improve registration accuracy. Next, to simulate fractional scanning, the projection data was sparsely subsampled to 0.6%, 1.2%, 1.8%, 2.4%, and 4.9% (6,12,18,24 and 48 respectively) of the 984 views at regular intervals in the range [0°, 180°], with a randomized offset angle to obtain a random subset of regularly spaced views. To allow compatibility with our rigid registration method which uses parallel beam data, we perform the needle localization on the same data using parallel beam geometry.
2) We used a full baseline scan of the phantom without the needle with the full dense sampling of view angles. We applied Radon-space rigid registration to each pair of baseline/repeat scans using the method described in [7]. The registration accuracy was evaluated as follows. First, we computed the transformed voxel coordinates using both the ground truth rigid transformation (based on image space registration between full baseline and repeat scans), and the Radon-space rigid transformation. Then, the registration error was computed as the RMS of differences between the transformed coordinates of the previous stage, across all phantom voxels. Results for global rigid registration error were in the range 0.32-0.75 mm.
3) We then calculated the needle orientation and marker position for each repeat scan as described in steps 3 and 4 above, using the needle-less scan as full baseline and needle modeled as a single straight segment. Fig. 5 illustrates graphically the resulting orientation, marker position and tip position for each scan.

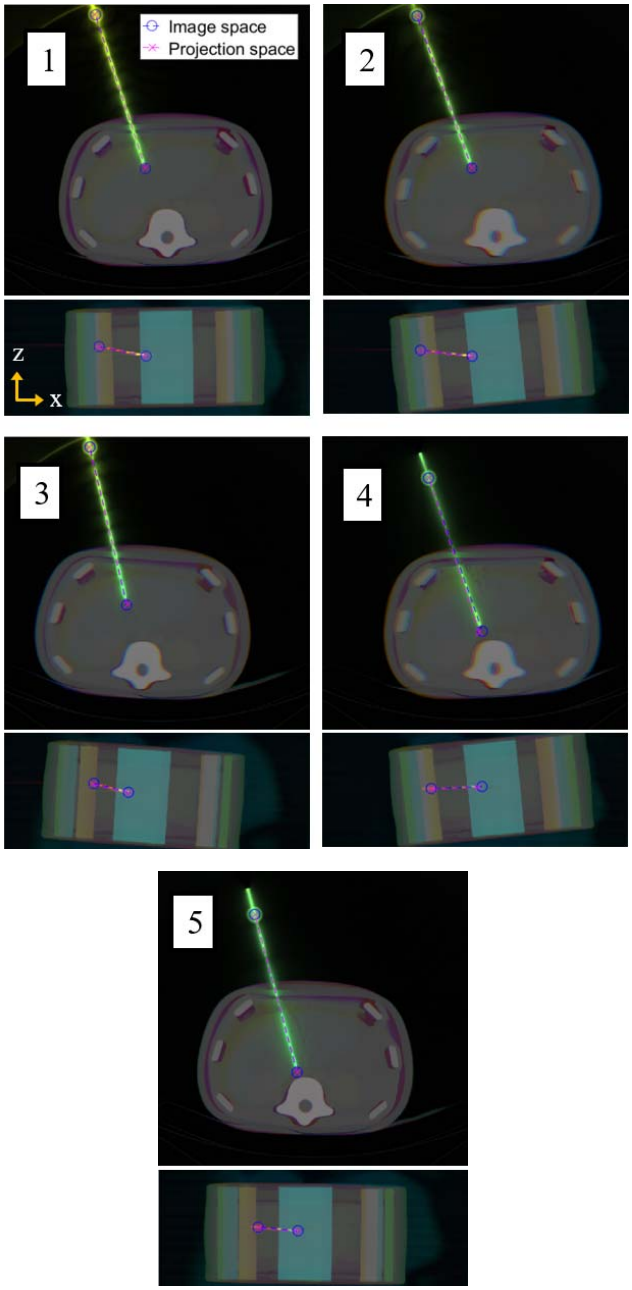

Fig. 5. Illustration of projection-space estimated needle position, vs. image-space estimated needle position in the 5 scans of the dataset displayed as multi-slice images. A multi-slice image is generated by assigning a color map to encode the depth of each slice in the direction perpendicular to the image plane. The needle is shown as a bright line in a multi-slice image in axial and coronal views (top row and bottom row, respectively). The needle localization is indicated as the circle and $\times$ marks at the ends of the colored lines, rep-resenting the marker center and tip position.

To validate our results, we performed image space needle localization as follows. Since the tip itself is obscured by reconstruction artifacts in the image, it cannot be localized directly in the reconstructed image. We therefore

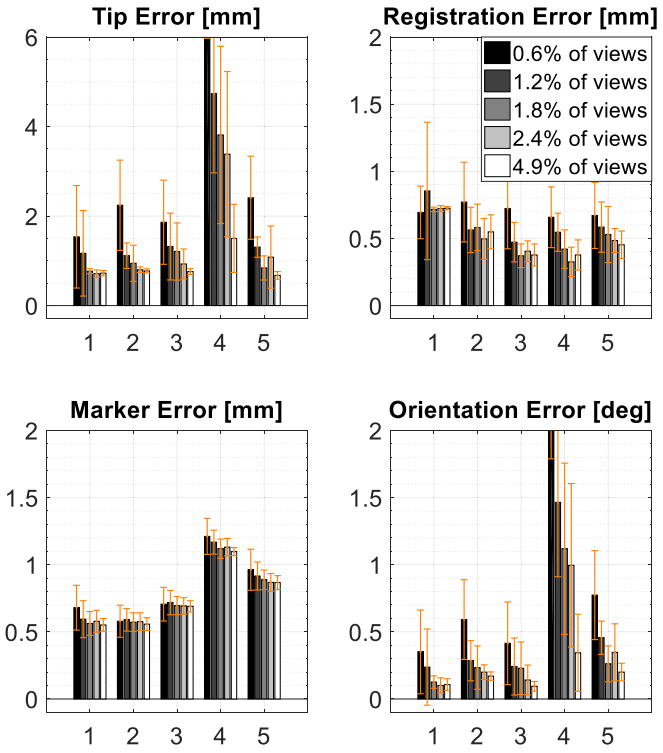

Fig. 6. Trade-off between the number of projections used as input to the needle localization algorithm and the achieved accuracy, with 0.6%, 1.2%, 1.8%, 2.4% and 4.9% of views (6/12/18/24/48 views respectively) for each of the 5 scans. In all scans 1-5, the tip error decreases when more projection views are used. This effect is mostly due to the orientation error which decreases with additional projection views. Scan 4 is seen to suffer from large orientation errors due to the shallow needle angle relative to the axial plane, requiring more views to reduce the orientation error (and therefore tip error) to acceptable levels.

localized the needle tip indirectly with the following procedure:

1) Localize the marker in image space using its spherical shape in 3D, in a similar fashion to the method used for each circular projection of the marker in 2D projection space.
2) Estimate the 3D orientation of the needle, in a similar fashion to the method used for each projection view of the needle in 2D projection space.
3) Localize the tip by tracing a ray along the calculated needle orientation from the calculated marker position, using the known distance between the marker and the tip.

The tip localization errors for the scans, as well as registration errors, orientation errors and marker localization errors, are shown in Fig. 6 per number of view angles used. The localization in each scan was repeated 45 times to account for randomization due to RANSAC scheme employed in different stages of the calculation and randomized angles selection.

Failure rates, defined as the percent of repetitions resulting in tip error above 3 mm, are shown in Table I. For 18 views and above, most failure cases are found in scan 4 and are due to a singular configuration in this scan: the angle between the needle and the axial plane is small (0.74°) where in all other scans the angle is 1.25° or larger, as can be seen in the coronal views in Fig. 5. This configuration, referred to as in-plane imaging of the needle, leads to reduced stability in the orientation calculation stage of the needle localization algorithm: geometrically, this is due to the intersecting planes depicted in Fig. 3 being nearly parallel to each other in this case. It can be observed from Fig. 6 and Table I that increasing the number of views reduces the localization error and failure rate. A choice of 24 view angles achieves a voxel-size tip localization error in scans 1, 2, 3 and 5, in which the needle is out of plane, and represents a compromise between dose reduction and required accuracy.

TABLE I
FAILURE RATE (TIP ERROR LARGER THAN 3mm) FOR EACH SCAN AND NUMBER OF VIEW ANGLES IN %. SCAN 4 SUFFERS FROM A HIGH FAILURE RATE DUE TO THE SHALLOW ANGLE OF THE NEEDLE

Scan # \ Views	6	12	18	24	48
1	13.3	11.1	0.0	0.0	0.0
2	33.3	0.0	0.0	0.0	0.0
3	13.3	0.0	0.0	0.0	0.0
4	100	80.0	62.2	42.2	6.7
5	31.1	0.0	0.0	4.4	0.0

The marker and orientation errors are dependent, which explains why the needle tip localization error may be smaller than the accumulated error resulting from both the marker center localization error and the needle orientation error. As described in Section III-D, we fit a 2D line through the detected marker center in each projection difference image so that the line coincides with the projection of the needle which appears as a bright thin line. The cost function minimization in Eq. (2) yields the needle orientation that counteracts the marker localization error because the needle is a line passing through the actual marker center, thereby reducing the cost in the direction that extends back towards the needle.

Note that while the proposed projection-space method and the validation image-space method are similar in nature, the latter requires the repeat scan to be fully available in order to reconstruct the image. We therefore demonstrate that both methods achieve comparable results, while the projection space method has the potential to significantly reduce the radiation dose required for each localization, compared with its image-space counterpart, via fractional scanning.

V. DISCUSSION

The key novelty of our method is the accurate location of a needle with respect to a patient anatomy in the CT scanner with sparse scan sampling and without reconstructing the CT image. The needle localization is performed directly in 3D Radon space using the raw sparse sinogram data produced by the CT scanner. The sparse sampling is achieved by fractional scanning. Based on the very limited number of views used by our methods to achieve registration and needle localization, we expect the reduction in radiation absorbed by the patient to be significant. Further research taking advantage of fractional scanning integrated into the CT scanning procedure would be required to assess the reduction quantitatively.

Fractional scanning consists of limiting the angular CT scanning range to intervals during scanning. Fractional scanning in a small range of few tenths of degrees is achievable with existing software and hardware by tube potential switching and tube current modulation. For example, tube current modulation is used in snapshot heart scanning to acquire 2-4 angular segments in adjacent heart cycles. Dual-voltage CT scanners switch the tube voltage between a higher voltage (140kV) and a lower voltage (80kV) every 1°. In inverse geometry CT [18], a proposed multiple source next generation CT architecture, the sources and detectors are fixed and only the collimators are rotating, raising the possibility of fractional scanning by limiting the number of active sources.

To implement our method on a commercial CT scanner, one of two methods can be used. The first method consists of modulating the voltage and tube current during the gantry rotation between a high value for acquisition and a low value at which the radiation density is limited – as a result, an absorbed X-ray dose reduction can be achieved. Alternatively, fast-switching mechanical collimation or redirection of the X-ray beam could achieve reduced dose, either in conventional or inverse geometry CT architecture. These methods require hardware integration at a level which is beyond the scope of this work. However, since the fraction of views required for successful localization by our method is below 5%, we estimate that given adequate solutions to CT hardware design challenges, the absorbed dose for needle localization can be reduced by one order of magnitude compared to a full acquisition aimed at image reconstruction.

Our method supports frequent, accurate needle tracking with respect to the patient, with no immobilization required. We note that the low accuracy obtained in the case of in-plane imaging of the needle can be mitigated by orienting the insertion to be out-of-plane, which is easier to accomplish than the in-plane requirement of some tracking methods.

The field of view necessary for the successful localization of the needle marker is determined by the distance from the tip, the angle of insertion, and the view angles scanned. In a worst case scenario, the needle is inserted at a large angle relative to the axial plane, with the marker affixed at a large distance. In this case, it is preferable to avoid acquiring the view angles for which the source is close to the marker, and use views acquired from the arc opposing the marker location, allowing the field of view to be narrower. In the experimental setup, where needle angles where in the range 0.75-3° out of plane, the field of view could be reduced without the marker and needle moving outside the view, as can be seen in Fig. 3 where the markers occupy only the central portion of the projections.

Running times of several minutes were recorded for each localization by our un-optimized implementation. Since the stage of needle and marker localization in projection space is independent between views and accounts for a majority of the execution time, an optimized implementation could feasibly lower it to a duration short enough to be acceptable for intra procedural use, especially if adapted to a GPU.

Our method is suitable when rigid registration is appropriate to align the baseline and the repeat scans, i.e., when tissue deformations are negligible (this does not apply to free breathing procedures). Our method requires a full dose baseline scan, assumes that the needle is rigid, and requires that the scan field of view includes the needle and the spherical marker and that the needle is imaged out-of-plane at an angle $>1.25°$. The expected advantages of our method over CT fluoroscopy are the increased accuracy of needle tip localization and the more significant dose reduction.

The straight needle localization method may be extended to a flexible needle as follows. The process involving point and line localization can be repeated by dividing the needle into short segments and establishing a sequence of points along the needle path such that the sum of segments length is equal to the known tip-marker distance. Further experimentation is required to verify the accuracy of this extension.

VI. Conclusion

We have described a new method for imageless needle and patient tracking in interventional CT procedures based on fractional CT scanning. Our method accurately locates a needle with a spherical marker attached to it at a known distance from the tip with respect to the patient in the CT scanner coordinate frame with online sparse scan sampling and without reconstructing the CT image.

The main advantages of our method are: 1) accurate needle orientation and needle tip localization without image reconstruction; 2) significant dose reduction for each individual snapshot due to much less radiation for the same amount of needle localizations and/or many more needle localizations for the same dose of radiation; 3) no in-plane needle location is required; 4) simultaneous patient registration and needle localization for every fractional CT scanning acquisition using the same sparse set of views; 5) fully automatic, no calibration and/or manual setup; 6) with the exception of a simple marker attached to the needle to determine its tip location, no additional hardware/setup is required; 7) artifact-free monitoring of needle location on top of a baseline scan; 8) supports closed-loop robotic flexible needle insertion.

Our experimental results indicate an accuracy level comparable to 3D image space methods, with the benefit of allowing X-ray dose reduction via fractional scanning at each localization. Fractional scanning is expected to yield a significant dose reduction since the number of scanning angles is one order of magnitude smaller than that of a full scan. The benefits of fractional scanning consist in the ability to perform either more frequent tip localizations during needle insertion for a similar total dose, or a reduced total dose for the same frequency of tip localization.

Acknowledgment

The authors thank Eyal Lin and Ronen Shter of GE Healthcare Israel for the CT scans and for their valuable assistance.

References

[1] E. J. Hall and D. J. Brenner, "Cancer risks from diagnostic radiology," *Brit. J. Radiol.*, vol. 81, no. 965, pp. 362–378, 2008.

[2] F. A. Mettler, Jr., P. W. Wiest, J. A. Locken, and C. A. Kelsey, "CT scanning: Patterns of use and dose," *J. Radiol. Protection*, vol. 20, no. 4, p. 353, 2000.

[3] H. E. Davies, C. G. Wathen, and F. V. Gleeson, "Risks of exposure to radiological imaging and how to minimise them," *Brit. Med. J.*, vol. 342, no. 7797, pp. 589–593, 2011.
[4] M. De Filippo *et al.*, "Predictive factors of diagnostic accuracy of CT-guided transthoracic fine-needle aspiration for solid noncalcified, subsolid and mixed pulmonary nodules," *La Radiol. Medica*, vol. 118, no. 7, pp. 1071–1081, 2013.
[5] R. Gupta, C. Walsh, I. S. Wang, M. Kachelrieß, J. Kuntz, and S. Bartling, "CT-guided interventions: Current practice and future directions," in *Intraoperative Imaging and Image-Guided Therapy*, F. A. Jolesz, Ed. New York, NY, USA: Springer, 2014, pp. 173–191.
[6] G. Medan, A. Kronman, and L. Joskowicz, "Reduced-dose patient to baseline CT rigid registration in 3D Radon space," in *Proc. Int. Conf. Med. Image Comput. Comput.-Assist. Intervent.*, 2014, pp. 291–298.
[7] G. Medan, N. Shamul, and L. Joskowicz, "Sparse 3D Radon space rigid registration of CT scans: Method and validation study," *IEEE Trans. Med. Imag.*, vol. 36, no. 2, pp. 497–506, Feb. 2017.
[8] O. Barkan, J. Weill, A. Averbuch, and S. Dekel, "Adaptive compressed tomography sensing," in *Proc. IEEE Conf. Comput. Vis. Pattern Recognit.*, Jun. 2013, pp. 2195–2202.
[9] Y. Liu, J. Ma, Y. Fan, and Z. Liang, "Adaptive-weighted total variation minimization for sparse data toward low-dose X-ray computed tomography image reconstruction," *Phys. Med. Biol.*, vol. 57, no. 23, pp. 7923–7956, 2012.
[10] S. Abbas, J. Min, and S. Cho, "Super-sparsely view-sampled cone-beam CT by incorporating prior data," *J. X-Ray Sci. Technol.*, vol. 21, no. 1, pp. 71–83, 2013.
[11] C. J. Walsh *et al.*, "Smaller and deeper lesions increase the number of acquired scan series in computed tomography-guided lung biopsy," *J. Thoracic Imag.*, vol. 26, no. 3, pp. 196–203, 2011.
[12] *NeoRad SimpliCT*. Accessed on Feb. 1, 2017. [Online]. Available: http://neorad.no/products_1/simplict_for_ct_and_pet_ct/
[13] T. Schubert, A. L. Jacob, M. Pansini, D. Liu, A. Gutzeit, and S. Kos, "CT-guided interventions using a free-hand, optical tracking system: Initial clinical experience," *Cardiovascular Intervent. Radiol.*, vol. 36, no. 4, pp. 1055–1062, 2013.
[14] G. Fichtinger *et al.*, "Image overlay guidance for needle insertion in CT scanner," *IEEE Trans. Biomed. Eng.*, vol. 52, no. 8, pp. 1415–1424, Aug. 2005.
[15] D. Glozman and M. Shoham, "Image-guided robotic flexible needle steering," *IEEE Trans. Robot.*, vol. 23, no. 3, pp. 459–467, Jun. 2007.
[16] F. E. Boas and D. Fleischmann, "CT artifacts: Causes and reduction techniques," *Imag. Med.*, vol. 4, no. 2, pp. 229–240, 2012.
[17] R. Hartley and A. Zisserman, *Multiple View Geometry in Computer Vision*. Cambridge, U.K.: Cambridge univ. Press, 2003.
[18] S. S. Hsieh *et al.*, "The feasibility of an inverse geometry CT system with stationary source arrays," *Med. Phys.*, vol. 40, no. 3, p. 031904, 2013.